Journal of Energy Chemistry 77 (2023) 290–299

Contents lists available at ScienceDirect

Journal of Energy Chemistry

journal homepage: www.elsevier.com/locate/jechem

http://www.journals.elsevier.com/journal-of-energy-chemistry/

Stable sodium anodes for sodium metal batteries (SMBs) enabled by in-situ formed quasi solid-state polymer electrolyte

Jian Ma [a,1], Xuyong Feng [a,1], Yueyue Wu [a], Yueda Wang [a], Pengcheng Liu [b], Ke Shang [c], Hao Jiang [a], Xianglong Hou [a], David Mitlin [b,*], Hongfa Xiang [a,*]

[a] School of Materials Science and Engineering, Anhui Provincial Key Laboratory of Advanced Functional Materials and Devices, Hefei University of Technology, Hefei 230009, Anhui, China
[b] Materials Science and Engineering Program & Texas Materials Institute (TMI), The University of Texas at Austin, Austin, TX 78712-1591, USA
[c] School of Chemistry and Chemical Engineering, Anhui Provincial Key Laboratory of Advanced Functional Materials and Devices, Hefei University of Technology, Hefei 230009, Anhui, China

ARTICLE INFO

Article history:
Received 1 September 2022
Revised 26 September 2022
Accepted 27 September 2022
Available online 03 October 2022

Keywords:
Quasi-solid batteries (QSBs)
Quasi-solid electrolytes (QSEs)
NaF-rich passivating layer
Interfacial stability
Sodium metal batteries (SMBs)

ABSTRACT

A high-performance quasi-solid polymer electrolyte for sodium metal batteries (SMBs) based on in-situ polymerized poly(1,3-dioxolane) (DOL) with 20% volume ratio of fluoroethylene carbonate (FEC), termed "PDFE-20", is proposed in this work. It is demonstrated PDFE-20 possesses a room-temperature ionic conductivity of 3.31×10^{-3} S cm^{-1}, an ionic diffusion activation energy of 0.10 eV, and an oxidation potential of 4.4 V. SMBs based on PDFE-20 and $Na_3V_2(PO_4)_3$ (NVP) cathodes were evaluated with an active material mass loading of 6.8 mg cm^{-2}. The cell displayed an initial discharge specific capacity of 104 mA h g^{-1}, and 97.1% capacity retention after 100 cycles at 0.5 C. In-situ polymerization conformally coats the anode/-cathode interfaces, avoiding geometrical gaps and high charge transfer resistance with ex-situ polymerization of the same chemistry. FEC acts as a plasticizer during polymerization to suppress crystallization and significantly improves ionic transport. During battery cycling FEC promotes mechanical congruence of electrolyte–electrode interfaces while forming a stable NaF-rich solid electrolyte interphase (SEI) at the anode. Density functional theory (DFT) calculations were also performed to further understand the role FEC in the poly(DOL)–FEC electrolytes. This work broadens the application of in-situ prepared poly(DOL) electrolytes to sodium storage and demonstrates the crucial role of FEC in improving the electrochemical performance.

1. Introduction

Sodium-ion batteries (SIBs) are attracted extensive research attention due to their potentially lower cost and improved sustainability over lithium-ion batteries (LIBs) [1–3]. In terms of electrochemical performance, SIBs lag behind LIBs both in their energy and power characteristics [4]. One promising option to achieve higher energy is to develop sodium metal batteries (SMBs) based on a Na metal anode and a ceramic high voltage cathode [5]. However, the high reactivity of Na metal results in poor electrochemical stability of the anode with conventional liquid electrolytes [6]. This brings both poor cycling performance and safety problems, preventing SMBs from being employed in any application. Battery failure may occur when the electrolyte continuously reacts with Na metal anode to consume the electrolyte to form the unstable solid electrolyte interphase (SEI) [7–9]. More sudden and potentially catastrophic failure can also occur from dendrite-induced internal short circuits [10]. Even more so than with conventional ion batteries, the leakage, burning and/or explosion of organic liquid electrolytes poses inherent safety risks for SMBs.

Solid-state electrolytes (SSEs) are attracting increasing attention due to their inherent safety characteristics such as non-flowability and nonflammability as well as the higher mechanical strength to potentially inhibit dendrite puncture [11–15]. However, a key deficiency is the poor physical contact between the rigid solid electrolyte and electrodes [16,17]. Geometrical gaps at the anode-SSE and cathode-SSE interfaces increase interfacial resistance remarkably and lead to large polarization. It will also result in localized variations in the current density, further degrad-

* Corresponding authors.
E-mail addresses: david.mitlin2@utexas.edu (D. Mitlin), hfxiang@hfut.edu.cn (H. Xiang).
[1] These authors contributed equally to this work.

https://doi.org/10.1016/j.jechem.2022.09.040

ing performance by triggering dendrites and parasitic reactions [18,19]. Approaches to alleviate these interfacial problems include creating organic–inorganic SSE composites [20–22], adding interfacial modification layers [23–25], alloying of the metal anode to enhance diffusion-based self-healing [26–28], integrated molding of the electrode and the electrolyte by solvent-casting [29,30], and in-situ polymerization to enhance interfacial contact [31,32]. Among these methods, the in-situ polymerization strategy can effectively eliminate geometrical gaps and possesses uniquely advantage in achieving intimate electrolyte–electrode contact simultaneously, greatly reducing interfacial resistances [33].

In a typical in-situ polymerization process, the liquid precursor containing salts, monomers, initiators and additives is injected into the battery as the substitute of liquid electrolyte. The battery will be post-processed (e.g., heated) to gradually transform the precursor into a solid state by the polymerization/crosslinking of monomers by initiators [33]. Systems demonstrating promising performance for sodium storage include poly(ethylene glycol) divinyl ether (PEGDE) [34], poly(ethylene glycol) methyl ether methacrylate (PEGMEMA) [35], pentaerythritol triacrylate (PETA) [36] and poly(vinylene carbonate) (PVC) [37]. The polymerization of these monomers usually requires a high temperature, e.g., 60–80 °C. However, such a heating process may bring some adverse effects, such as the decomposition of precursor and the accelerated side reactions between electrolyte and metal anode, especially in view of the high chemical reactivity of Na metal [38]. A room temperature polymerization process would therefore be desirable. The cyclic ether monomer 1,3-dioxolane (DOL) is gaining attention for lithium metal and lithium sulfur batteries, being able to be ring-opening polymerized at room temperature [39–47]. The poly (DOL)-based electrolytes possess merits of high ionic conductivity and good compatibility towards lithium metals [45,48]. Notwithstanding, the application of poly(DOL)-based electrolytes in SMBs is rarely reported.

The in-situ polymerized electrolytes are polymer-based [49]. Although polymer electrolytes improve safety with better thermal stability, lower flowability and volatility, the ionic conductivity at room temperature and the interface conduction between electrolytes and electrodes are still unsatisfactory. Moreover, due to the volume changes at the anode (and potentially at the cathode), it remains a challenge to maintain this geometrical matching during cycling, as the electrolyte no longer flows to fill in the gaps and the perturbations [50,51]. Hence while at cycle one the geometrical matching is nearly perfect, with extended cycling this interfacial congruence is lost [52]. An effective but compromise solution is the incorporation of small amounts of liquid phase to form the quasi-solid electrolyte. Having some liquid phase is advantageous in terms of promoting fast ionic conduction and maintaining good interfacial wettability, and at the same time the good safety of solid-state electrolyte is inherited [53–58].

In addition, the deteriorated interface in solid-state SMBs may be also originated from continued interfacial side reactions at the high-active Na metal anode side. Many strategies have been proposed to stabilize Na metal anodes, which can be generally divided into electrolyte-based strategies (e.g., film-forming additive [59]) and anode-based strategies (e.g., anode framework [60] and metal alloying [61,62]). The electrolyte-based strategies are highly compatible with in-situ polymerization process, because additives/co-solvents can be facilely and directly incorporated into the electrolyte precursor.

Here, we develop a novel DOL-based quasi-solid electrolyte for SMBs, in which the ring-opening polymerization of DOL is initiated by a small amount of Lewis acid aluminum trifluoromethanesulfonate ($Al(OTf)_3$), while fluoroethylene carbonate (FEC) is included as a performance-enhancing additive. The addition of FEC not only enhances the ionic conductivity of poly(DOL) electrolyte, but also improves the integrity of the electrolyte–electrode interface. A NaF-rich SEI layer forms on the Na metal anode, which blocks the ongoing reaction of Na metal with DOL, homogenizes the electroplating-eletrodissolution process, and effectively inhibits the growth of dendrites. This in-situ prepared poly(DOL)-based electrolyte is successfully applied in SMBs that employ high-mass loading $Na_3V_2(PO_4)_3$ (NVP) cathodes. The electrochemical performance of the electrolyte and of the SMBs is analyzed in detail, with state-of-the-art being achieved.

2. Results and discussion

The schematic process of the in-situ polymerization preparation of polymer electrolytes is illustrated in Fig. 1(a). In general, the liquid precursor containing monomers (DOL) and initiators ($Al(OTf)_3$) is injected into the battery, and the assembled battery is rested at room temperature for the gradually polymerization and solidification of the precursor. With this in-situ process, liquid precursor will wet cathode and anode interfaces, creating an intimate interfacial contact with both. After polymerization and solidification, these intimate contacts are preserved. Fig. 1(b) shows the digital paragraphs of different polymer electrolytes. For brevity, abbreviations are used to represent different electrolytes. The abbreviation "LDE" (liquid DOL electrolyte) denotes liquid 1 M NaTFSI/DOL electrolyte. Another baseline "LFE" represents a liquid 1 M NaTFSI/FEC electrolyte, which is analyzed by NMR and FT-IR only. The abbreviation "PDE" (poly(DOL) electrolyte) denotes polymerized 1 M NaTFSI/DOL electrolyte prepared by the addition of 0.5 mM Al $(OTf)_3$ initiator. The abbreviations "PDFE-5" and "PDFE-20" (poly (DOL)–FEC electrolytes) represent polymerized 1 M NaTFSI/DOL-FEC (95:5, *v*:*v*) and 1 M NaTFSI/DOL–FEC (80:20, *v*:*v*) electrolytes, prepared by the addition of 0.5 mM $Al(OTf)_3$ initiator.

Although the prepared electrolytes are primarily in the form of a solid that cannot flow freely, there are significant differences between them. PDE is crystallized and consequently opaque, while being fully rigid. By contrast PDFE-20 is transparent with limited flow. PDFE-5 exhibits an intermediate structure, meaning that a portion of it is crystallized while a portion of it is not. As shown in Fig. S1, the growth of polymer crystals in PDE is observed after holding for 8 h at room temperature, with nearly complete crystallization occurring after another 24 h. In solid polymer electrolytes, crystallization is undesirable [63]. The introduction of FEC as plasticizer reduces the crystallinity of poly(DOL) and is therefore beneficial to the improvement of ionic conductivity. To balance the plasticizing effect with the generation of unnecessary excess liquid, the maximum addition of FEC was 20% by volume. A scanning electron microscope (SEM) image and the corresponding EDXS maps of as-prepared PDFE-20 is shown in Fig. 1(c). A glass fiber frit is used as the support for the electrolyte, with maps of Si, Al and O illustrating the position of the fibers. It may be observed that electrolyte has flowed around the fiber frit and now possesses a relatively smooth surface.

The chemical structures of the poly(DOL)-based electrolytes were characterized. Fig. 2(a) schematically illustrates the cationic ring-opening polymerization process of DOL initiated by $Al(OTf)_3$. The bond breakage and chain growth are highlighted. Fig. 2(b) provides the nuclear magnetic resonance (NMR) results for the different electrolytes. For the LDE electrolyte, the peak at 4.75 ppm in ^1H NMR spectra corresponds to the H on the –O–CH_2–O– structure. The peak at 3.75 ppm is assigned to the group —O—CH_2—CH_2—O—. In ^{13}C NMR spectra, the peak at 95.18 ppm represents to the C on the group —O—CH_2—O—, and at 66.45 ppm corresponds to the —O—CH_2—CH_2—O— structure [45,64]. In the PDE, PDFE-20 and PDFE-5 samples, chemical shifts in these hydrogen and carbon signals are present due to the poly-

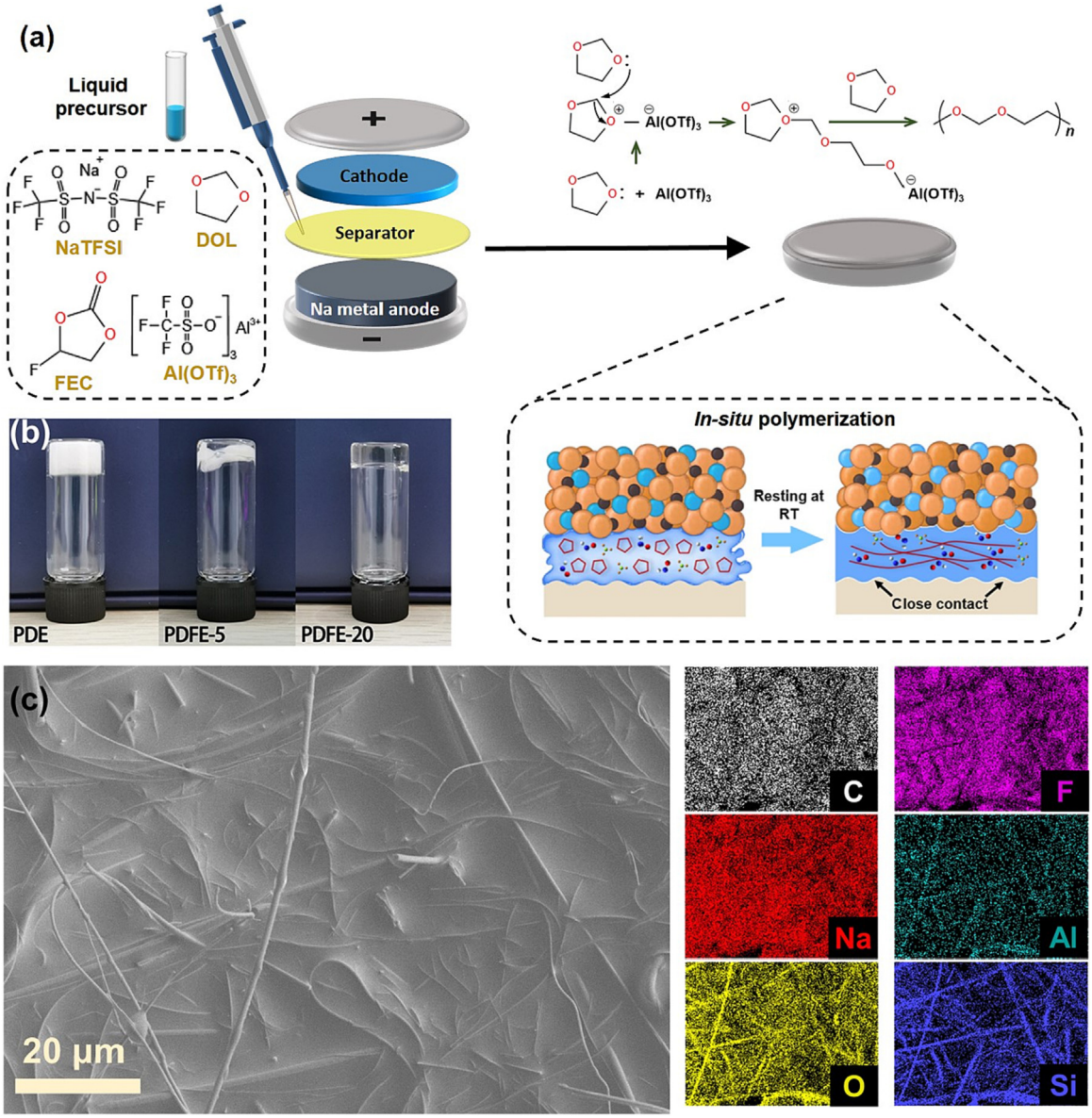

Fig. 1. (a) Schematic illustration of the in-situ polymerization preparation of the poly(DOL)-based polymer electrolyte. (b) Photographs of the three prepared electrolytes (PDE, PDFE-5 and PDFE-20). (c) An SEM image and the corresponding EDXS maps of as-prepared PDFE-20 that is supported on a glass fiber frit.

merization corresponding to the formation of poly(DOL) structure. However, small peaks attributed to liquid DOL are still detectable. This indicates that as expected, the liquid DOL does not completely polymerize. By integrating the respective peak area of ^{1}H NMR spectra, the ratio of polymerized DOL to total DOL content can be estimated [45]. These results are shown in Table S1. The addition of liquid plasticizer reduces the polymerized DOL ratio. In PDFE-5 and PDFE-20 polymerized DOL monomers account for 83.6% and 91.7%, respectively, which is lower than the 95.4% in PDE. Such remnant liquid will contribute to rapid Na^+ transport inside the quasi-solid electrolyte. The above polymerized DOL ratios are comparable or somewhat higher than those of prior reports on in-situ polymerization of DOL [45–47]. The peak at 72.13 ppm in ^{13}C NMR spectra is attributed to group —CH_2—O— of FEC. The position of this peak remains unchanged in all FEC-containing samples, indicating that FEC still maintains a liquid state [65]. The Fourier transformed infrared (FI-IR) spectra of different electrolytes is plotted in Fig. 2(c). The —C—O—C— peaks at 1020 and 1082 cm^{-1} and the C—H out of plane peaks at 915 cm^{-1} attenuate after polymerization, indicating bond breakage in DOL. An absorption peak at 848 cm^{-1} emerges after polymerization, proving the formation of poly(DOL) [45].

Gel permeation chromatography (GPC) measurement was performed to determine the weight-averaged molecular weight (M_w) of poly(DOL) chains in different electrolytes. Results are plotted in Fig. S2 and summarized in Table S1. The PDE electrolyte has a weight-averaged molecular weight of 7.8 kDa. With the addition of 5% volume ratio of FEC, the M_w of chains remains almost unchanged at 7.7 kDa. With the increase of FEC content to 20%, the M_w significantly decreases to 4.1 kDa. The FEC molecules inset between DOL molecules, reducing the mutual contact probability and interactions (e.g., van der Waals force) between DOL molecules to a certain extent. Therefore, the polymer properties including the averaged molecular weight are unavoidably influenced. Nonetheless, the 5% addition content is not enough to restrain the growth of long chains once cationic polymerization has been triggered. The addition of 20% FEC obviously inhibits the polymerization of monomers and hinders the growth of long chains. This demon-

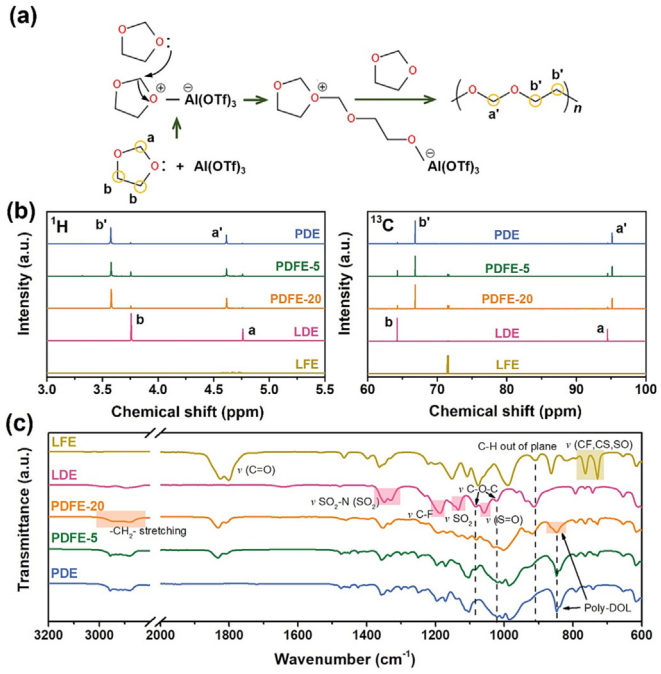

Fig. 2. (a) Chemical reaction schematic illustrating the polymerization process of DOL initiated by $Al(OTf)_3$. (b) ^{1}H and ^{13}C NMR spectra of these electrolytes as well as the LDE and LFE (liquid 1 M NaTFSI/FEC electrolyte) baselines. (c) FT-IR spectra of the different electrolytes.

strating the significant role of FEC in determining the final structure of the electrolyte.

Thermogravimetric analysis (TGA) was carried out on the different electrolytes. As shown in Fig. S3, the LDE continuously losses weight at room temperature due to its low boiling point of 76 °C. After polymerization of DOL, PDE maintains thermal stability up to approximately 120 °C (Fig. 3a). In Fig. 3(b), the PDFE-20 sample also displays good thermal stability up to 100 °C (only 3% weight loss), much better than that of the LDE. It should be noted that the endothermic peaks of poly(DOL) and poly(DOL)–FEC electrolytes are dissimilar. Owing to the different molecular weight of polymer chains, the decomposition of polymers is usually distributed in a range. For PDE, the endothermic peaks at 70 °C correspond to the decrystallization of poly(DOL). The peaks at 127 °C and 198 °C correspond to the decomposition of low molecular poly(DOL) (oligomers) and high molecular poly(DOL), respectively. These results are illustrated in the GPC plot shown in Fig. S2. Similar trend can be found with the PDFE-5 sample, as shown in Fig. S3. For PDFE-20, owing to the reduced crystallinity of poly (DOL), the endothermic peak at 70 °C is not obvious. Rather, the more compact distribution of molecular weights results in a single endothermic peak at 168 °C. This further illustrates the role of FEC in affecting the polymerization process.

Symmetric stainless steel (blocking electrode) cells were employed to measure the ionic conductivity of the different electrolytes using electrochemical impedance spectroscopy (EIS). The Nyquist plots of PDE, PDFE-5 and PDFE-20 at different temperatures are shown in Fig. S4. Their variation of ionic conductivity with temperature is plotted in Fig. 3(c), with the trend following an Arrhenius relation. The ionic conductivity of the PDFE-20 electrolyte reaches 3.31×10^{-3} S cm^{-1} at 25 °C. As calculated from the Arrhenius Equation (Eq. S2), the ionic diffusion activation energy E_a is 0.10 eV. By comparison, the ionic conductivities of PDFE-5 and PDE are 1.61×10^{-3} S cm^{-1} and 4.98×10^{-4} S cm^{-1}, respectively. Their activation energies are 0.19 eV and 0.25 eV. It is therefore evident that the addition of FEC has a major effect on the ionic conductivity in the electrolytes. It also indicates that majority of the Na^+ diffusion paths are inside the liquid FEC additive and in the unpolymerized liquid DOL component, rather than in the poly(DOL) skeleton. The viscosity and solvation structure inside the solid electrolyte will also have some influence on the conductivity. The introduction of FEC as plasticizer inhibits the crystallization and improves the activity of the polymer chains, which is advantageous for the diffusion of ions. The variation of ionic conductivity versus time is shown in Fig. S5. With both PDE and PDFE-20 the ionic conductivity undergoes a drastic decrease during the first 20 h and gradually becomes stable after about 50 h, showing that the addition of FEC has limited influence on the polymerization rate.

Linear sweep voltammetry measurement was employed to compare the electrochemical stability of the different electrolytes. The results are shown in Fig. 3(d). It is well-known that cyclic ether solvents are unstable at high voltages. The LDE oxidizes at 3.6 V vs. Na/Na^+, while the PDE is stable up to 4.6 V, indicating that polymerization of DOL improves its electrochemical stability. The PDFE-5 and PDFE-20 samples display an incrementally lower oxidation potential at 4.4 V. It is reasonable that the slightly increased unpolymerized DOL in PDFE-20 is unstable, which accelerates the oxidation under high voltage. Nonetheless, the oxidation stability of PDFE-20 is much better than LDE, greatly expanding the applicable scope. Nyquist impedance spectra of the different electrolytes in Na||Na symmetrical cells are plotted in Fig. 3(e), tested after storage at room temperature for 2 days after assembly. The PDFE-20 electrolyte displays the lowest interfacial resistance (592 Ω), while the PDE electrolyte has the highest (>4000 Ω). According to Fig. 3(f), the interfacial resistance of PDFE-20 is relatively stable with extended room temperature aging, being 486 Ω after 24 h, 592 Ω after 2 days, 640 Ω after 30 days, and 636 Ω after 45 days. It is known that poly(DOL) will form a solid reaction layer when in contact with lithium metal [66–68]. It will also transform by electrochemical polymerization [69,70]. The interfacial resistance between poly(DOL) and lithium metal has been reported to be at or below 300 Ω [45,46]. The somewhat higher interfacial resistance of PDFE-20 with Na metal may be attributed to the higher intrinsic reactivity of sodium versus lithium. Due to its larger atomic size and hence a less strongly bound valence electron, a sodium atom is more reactive than a lithium atom. The reaction layer may be therefore thicker (and possibly less ironically conductive) with sodium, impeding charge transfer at the interface. Fig. S7 shows such EIS analysis for the LDE electrolyte. It may be observed that there is a rapid rise in interfacial resistance due to the reaction of LDE with the Na metal. Moreover, the interfacial resistance continually increases, reaching 10^5 Ω after 80 days. This result supports the argument that it is the remnant liquid in the poly(DOL) that is the most reactive with the sodium and that FEC suppresses this ongoing reaction.

Density functional theory (DFT) calculations of frontier molecular orbital energies were performed to further understand the interfacial stabilization mechanism of FEC. It is reported that the lowest unoccupied molecular orbital (LUMO) and the highest occupied molecular orbital (HOMO) of the ion–solvent complexes are very likely lower than those of the pure solvents [71,72]. Hence the LUMO and HOMO of DOL, Na^+-DOL, FEC and Na^+-FEC were all compared. The visual LUMOs and HOMOs are presented in Fig. S8 and the calculated results are summarized in Table S2. The Na^+-FEC ion–solvent complex has its LUMO (−0.61 eV) below that of FEC (−0.15 eV), DOL (0.21 eV) and Na^+-DOL (−0.53 eV). This makes Na^+-FEC more prone to be reduced at the surface of Na anode. The reduction of Na^+-FEC is responsible for the stable layer that blocks the further reaction between DOL and Na metal. The HOMO of DOL (−6.99 eV) and Na^+-DOL (−7.53 eV) is above that of FEC (−9.09 eV) and Na^+-FEC (−9.58 eV). This indicates that the

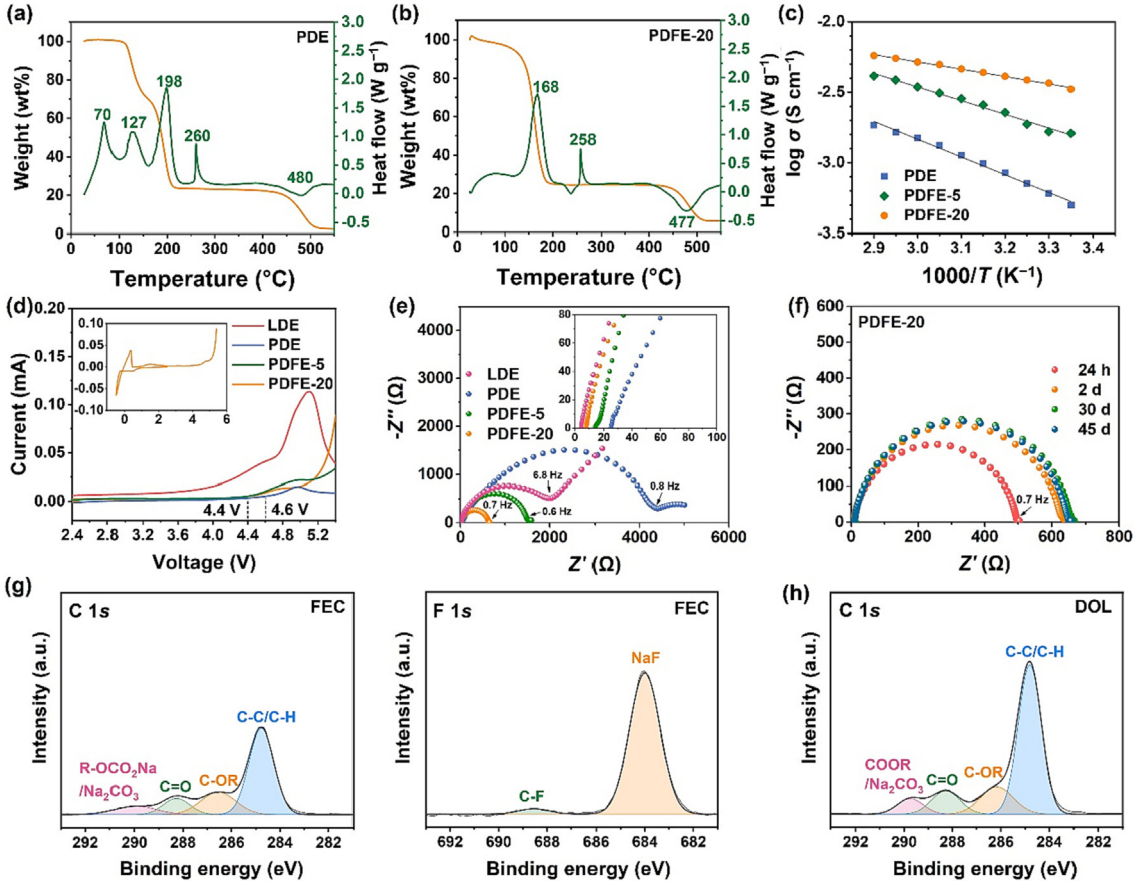

Fig. 3. (a and b) Thermogravimetric (TGA) and differential scanning calorimetry (DSC) curves of PDE and PDFE-20, respectively. (c) Variation of ionic conductivity with temperature for the different electrolytes obtained from symmetric cells with blocking stainless steel electrodes. (d) Comparison of linear sweep voltammetry (LSV) curves for the different electrolytes. (e) Comparison of Nyquist impedance spectra of the different electrolytes tested in symmetric Na||Na cell configuration, tested at 2 days after assembly. (f) Nyquist spectra of symmetric Na||Na cells with PDFE-20 as a function of storage time, 24 h to 45 days after assembly. (g) XPS analysis of Na metal soaked in FEC for 3 days, displaying the C 1*s* and F 1*s* spectra. (h) XPS analysis of Na metal soaked in DOL for 3 days, displaying the C 1*s* spectrum.

DOL molecule and Na^+-DOL is more prone to be oxidized at the cathode than FEC and Na^+-FEC. This explains why pristine liquid DOL electrolyte oxidizes at 3.6 V vs. Na/Na^+, while FEC-based liquid electrolytes have been reported stabilities above 4 V vs. Na/Na^+ [73–75].

To further understand the reaction products, XPS analysis was carried out on Na metal anodes surfaces soaked for 3 days in FEC or in DOL. The results are shown in Fig. 3(g and h). In the C 1*s* spectrum of the FEC sample, peaks attributed to common carbon bonds including C—C/C—H, C—OR and C═O are present. Moreover, a peak at 290.0 eV is present, which is associated with R—OCO_2Na and Na_2CO_3. This indicates a ring-opening decomposition and/or radical recombination of FEC molecular induced by high-active Na surface [76]. A significant NaF signal at 683.9 eV in the F 1*s* spectrum is detected on the surface of the FEC sample. The NaF-rich SEI is known to promote enhanced ionic transport, as well as improved interfacial stability that prevents further side reactions with electrolyte [74,77]. This NaF-rich layer is possibly formed from the direct contact between the FEC and Na^+, and may also originate from the defluorination of FEC under the catalytic effect of the Na metal, where the produced HF reacts with Na metal to generate NaF [76]. The reaction products from DOL are mainly organic components containing C—C, C—O, C═O bonds and CO_3^{2-}, COOR groups. These should originate from the ring-opening degradation of DOL by the reaction with Na metal [78]. The O 1*s* spectra of FEC and DOL are shown in Fig. S9. The peak belonging to R–OCO_2Na at 532.9 eV is found in the FEC sample but not in the DOL sample, which is in accordance with the C 1*s* spectra.

The interfacial stability and dendrite inhibition property can be evaluated by the cycling performance employing the symmetrical Na||Na cells (Fig. 4). In Fig. 4(a) the symmetrical cell employing PDE displays a large overpotential (>0.3 V) at a current density of 0.5 mA cm^{-1}. During the plating and stripping process the overpotential continuously grows, indicating geometrically and/or electrochemically unstable interfaces. The overpotential sharply increases at 57 h. This is associated with loss of physical contact and/or severe SEI growth. With a rigid electrolyte, such as PDE, the volume changes of the metal anode associated with plating and stripping will lead to geometrical gaps that enlarge with time. Limited cycling remains possible due to some physical contact being maintained, but with growing localized electrical field-current density concentration and accelerated growth of reaction layers. The geometrical separation at the interface and the reaction layer buildup are likely to be negatively synergistic, with one accelerating the other and vise-versa. In studies of LiTFSI/poly(DOL) and lithium anodes the overpotential at the same current density is lower (<0.1 V) [45,46], with more stable cycling being reported. This agrees with the earlier discussion regarding the more severe interfacial reactivity of various polymer electrolytes with sodium metal versus with lithium.

Studies have also demonstrated that Na-metal employing DOL-based electrolytes undergo greater degree of dendrite growth than

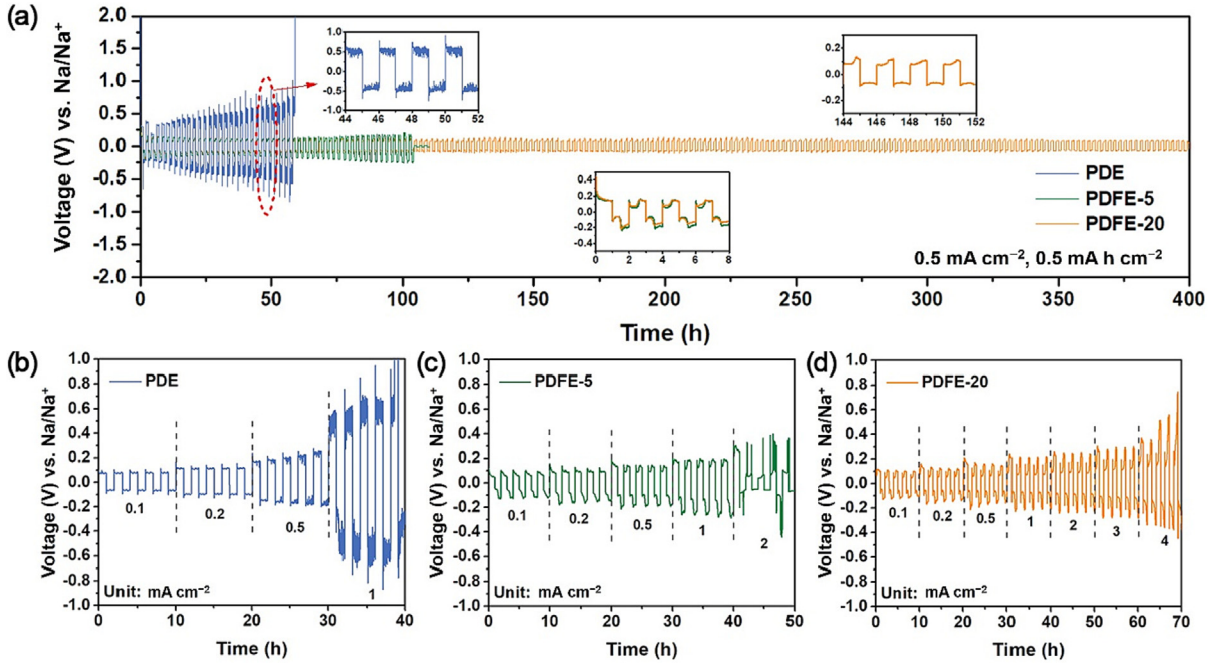

Fig. 4. Electrochemical performance of PDE, PDFE-5 and PDFE-20 electrolytes tested in symmetrical Na||Na cells. (a) Long-term cycling performance, at current density of 0.5 mA cm^{-2} with 0.5 mA h cm^{-2} capacity per cycle. (b–d) Cycling at increasing current densities, with five plating-stripping cycles per current.

their lithium counterparts [79]. The transient short circuit shown in the inset of Fig. 4(a) for the PDE sample is an example of dendrite-driven failure. Transient self-healing does occur with the specimen being able to cycle for a brief period longer before terminally short circuiting. This effect is known, being associated with current reversal leading to dissolution or physical separation of the dendrite tip that was in contact with the opposite electrode. Greatly improved cycling stability is obtained through the addition of FEC, especially for PDFE-20. At the same current density, the plating/stripping overpotential is reduced to <0.15 V while cycling stability is maintained. The cell based on PDFE-20 stably runs for over 400 h, while a short circuit occurs at 105 h for PDFE-5. Fig. 4(b–d) display the cycling performance of PDE, PDFE-5 and PDFE-20 with increasing current density, with five plating-stripping cycles per current. For cells employing PDE the maximum current density is 0.5 mA h cm^{-2}, and for PDFE-5, it is 1 mA h cm^{-2}. Employing PDFE-20 the symmetric cell can stably cycle at 3 mA h cm^{-2}. The improvement with 20% versus 5% FEC can be directly attributed to several synergistic effects: these include improved geometrical contact due to less crystallization and more liquid being present, increased SEI stability due to more F being available to form NaF on the metal anodes, and an overall higher ionic conductivity that should directly lead to more facile electrodeposition/electrodissolution kinetics.

The surface of the cycled Na was extracted from the PDE and PDFE-20 symmetrical cells and analyzed by SEM. Those results are shown in Fig. 5(a and b), respectively. Since both photographs were taken with the disassembled and cleaned anodes being kept inside the inert atmosphere glove box, the surfaces observed underwent minimal post-mortem oxidation. It may be observed that the surface of the PDE specimen is highly roughened. The roughening is due to the poor interface between PDE and Na metal, in which the diffusion of Na^+ ions and plating of Na metal are both uneven [61]. The metal roughening in the PDE sample will deteriorate the interface leading to loss of physical contact, localized current "hot spots" at the remaining contacting regions, and possible dendrites that lead to electrical short circuits. It may be observed that the FEC present in PDFE-20 improves the geometrical stability interface between polymer electrolyte and Na metal anode. A fast and uniform Na^+ flux through the NaF-rich SEI would have this effect, as would the ongoing presence remnant liquid in the electrolyte. It is known that NaF within the SEI promotes rapid solid-state ion diffusion [80], which should increase the critical current for metal dendrite and metal void formation. The electroplated Na metal in symmetrical cells with PDFE-20 were analyzed further. Capacities of 1 mA h cm^{-2}, 3 mA h cm^{-2} and 5 mA h cm^{-2} were deposited at 1 mA cm^{-2}. The SEM analysis of these surfaces is shown in Fig. S10. While surface unevenness does occur at higher capacities, there is no evidence for dendrite formation.

The post-cycled anodes were further analyzed by XPS to reveal the differences in SEI compositions. Fig. 5(c and d) show this analysis for the PDE and PDFE-20 samples respectively, illustrating the high-resolution C 1*s*, O 1*s* and F 1*s* peaks. For the PDE sample, the binding energy peaks in C 1*s* and O 1*s* spectra indicate the formation of C—C, C—OR, C=O, COOR and Na_2CO_3 components in the SEI. These primarily originate from the decomposition of DOL. In the F 1*s* spectra, minimal C—F and Na—F peaks are detected, which would originate from the decomposition of NaTFSI containing —CF_3 group during cycling. For the PDFE-20 anode, much stronger C—F and Na–F peaks are present in the F 1*s* and C 1*s* spectra. The C—F bond mainly comes from the Na metal-induced ring-opening decomposition of FEC during cycling that generates CH_2=CHF (and further the polymerization of CH_2=CHF to —[CH_2—CHF]$_n$—) and CH_3—CHF—OCO_2Na (R—OCO_2Na, R = CH_3—CHF) [76,81]. The R—OCO_2Na peak is also found at 289.3 eV in the C 1*s* spectrum, as well as at 532.9 eV in the O 1*s* spectrum. It should be noted that for the Na metal soaked in FEC for 3 days (Fig. 3g), no obvious C—F peak is observed, indicating that formation of CH_2=CHF and CH_3—CHF—OCO_2Na is a reduction process that requires external electrons. It is reasonable to argue based an established body of literature [74,77,82], that it is the formed NaF layer in PDFE-20 that is key for enhanced interfacial stability.

Batteries employing NVP as the cathode (1.12 mg cm^{-2}) and Na metal as the anode were tested with different electrolytes. Fig. 6(a)

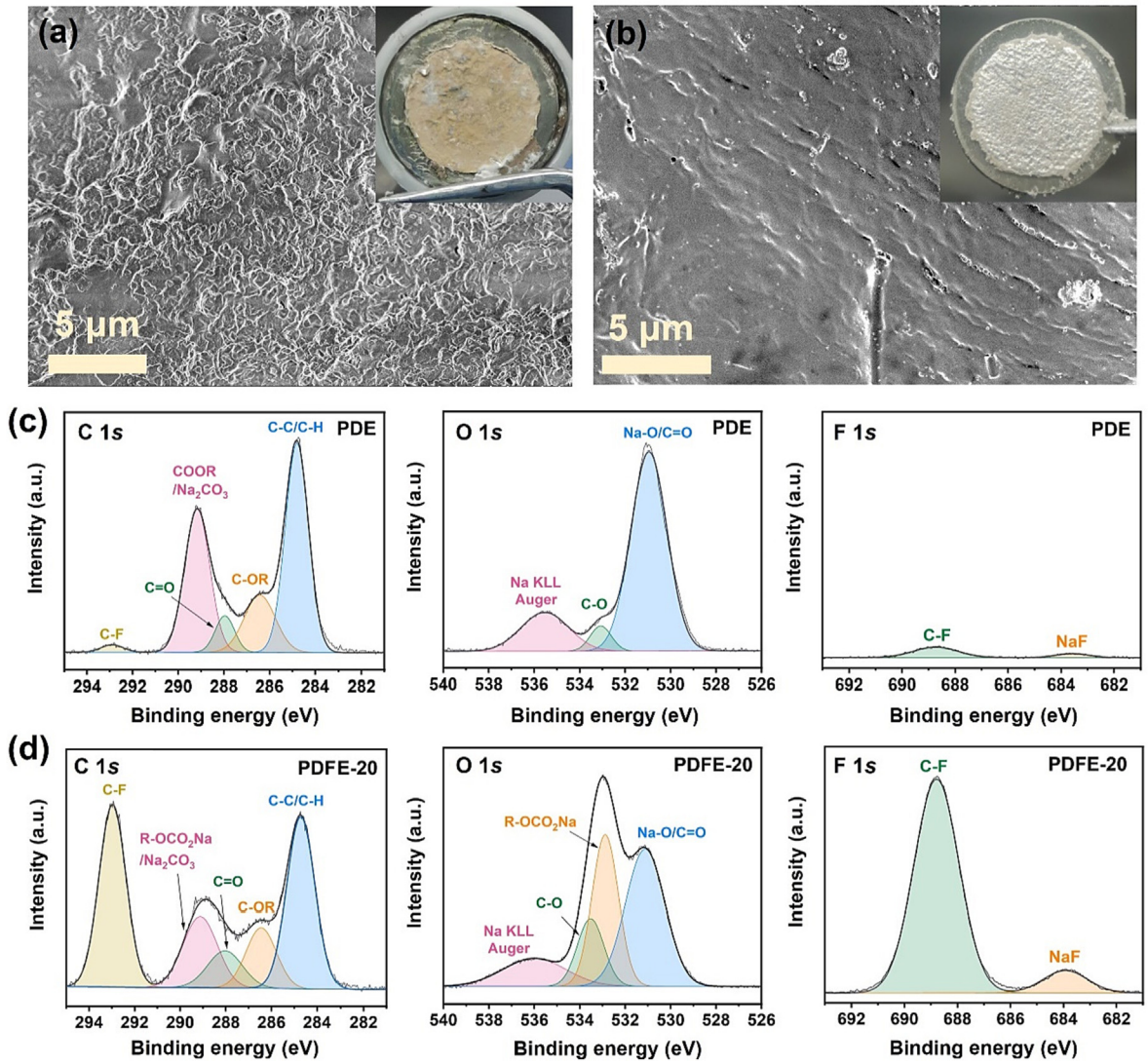

Fig. 5. (a) SEM images and macroscopic optical photographs (inset) of the Na metal surface of the post-cycled Na|PDE|Na symmetric cell (both after 100 cycles at 0.2 mA cm^{-2}, 0.2 mA h cm^{-2}). (b) Same analysis but for PDFE-20. (c) XPS analysis of post-cycled Na metal with PDE, showing the high-resolution C 1*s*, O 1*s* and F 1*s* peaks. (d) Same analysis but for PDFE-20.

provides a comparison of rate performance with PDE, PDFE-5 and PDFE-20 (1 C = 117 mA h g^{-1}). The battery with PDE is inferior to the other two electrolytes at every rate tested. At the lower rates, the PDFE-20 specimen performs on par to PDFE-5. However, at 0.5 C and above, the cell employing PDFE-20 is progressively superior. With PDFE-20, a discharge capacity of 88.3 mA h g^{-1} is obtained at 10 C. This effect is attributed to the enhanced ionic conductivity and the improved geometrical congruence with 20% versus 5% FEC. Enhanced electrochemical stability of the electrode–electrolyte interfaces due to more FEC being available to form NaF is another key factor. Per Fig. 6(b), the cell employing PDE has a very large polarization during the charge/discharge processes, e.g., >0.6 V at 0.5 C rate. As shown in Fig. 6(c), the cell employing PDFE-20 possesses substantially reduced polarization and the resultant increased specific capacity at the same rate.

The PDE electrolyte has large interfacial resistance and leads to large polarization and poor rate performance. However, even compared with the liquid DOL-based electrolyte (LDE), PDFE-20 still shows better performances. Fig. 6(d) plots the battery galvanostatic cycling performance with PDFE-20 and LDE, tested at 0.5 C. After 50 cycles, the Coulombic efficiency of the cell employing LDE begins to fluctuate while the discharge capacity retention rapidly decreases. This degradation is driven by the reactions at the anode-electrolyte interface as well as at the cathode-electrolyte interface, since LDE is not stable above 3.6 V. By contrast, stable cycling is achieved with PDFE-20 electrolyte. Fig. 6 (e) shows the charge/discharge curves at different cycle numbers with PDFE-20. The cell shows an initial discharge specific capacity of 107 mA h g^{-1} and a Coulombic efficiency (CE) of 96.75%. After 600 cycles the cell possesses a capacity retention of 96.7% and with a stable CE of >99.5%), further demonstrating cycling stability of the cell is the relatively unchanging impedance behavior. Fig. 6(f) plots the Nyquist impedance spectra at different cycle numbers for the PDFE-20 cell. Before cycling the cell has an Ohmic resistance of 7.2 Ω and an interfacial charge transfer resistance R_{ct} of 545 Ω. After 100 cycles at 0.5 C, a semicircle corresponded to SEI resistance emerges, which has a value of 33 Ω. The interfacial charge transfer resistance, however, is significantly reduced to 279 Ω. This phenomenon supports the argument that FEC contributes to the formation of NaF-rich SEI layer on anode surface during cycling, leading to improved interfacial Na^+ transfer kinetics and lowered interfacial resistance. From the 100th to 600th cycle, the SEI inter-

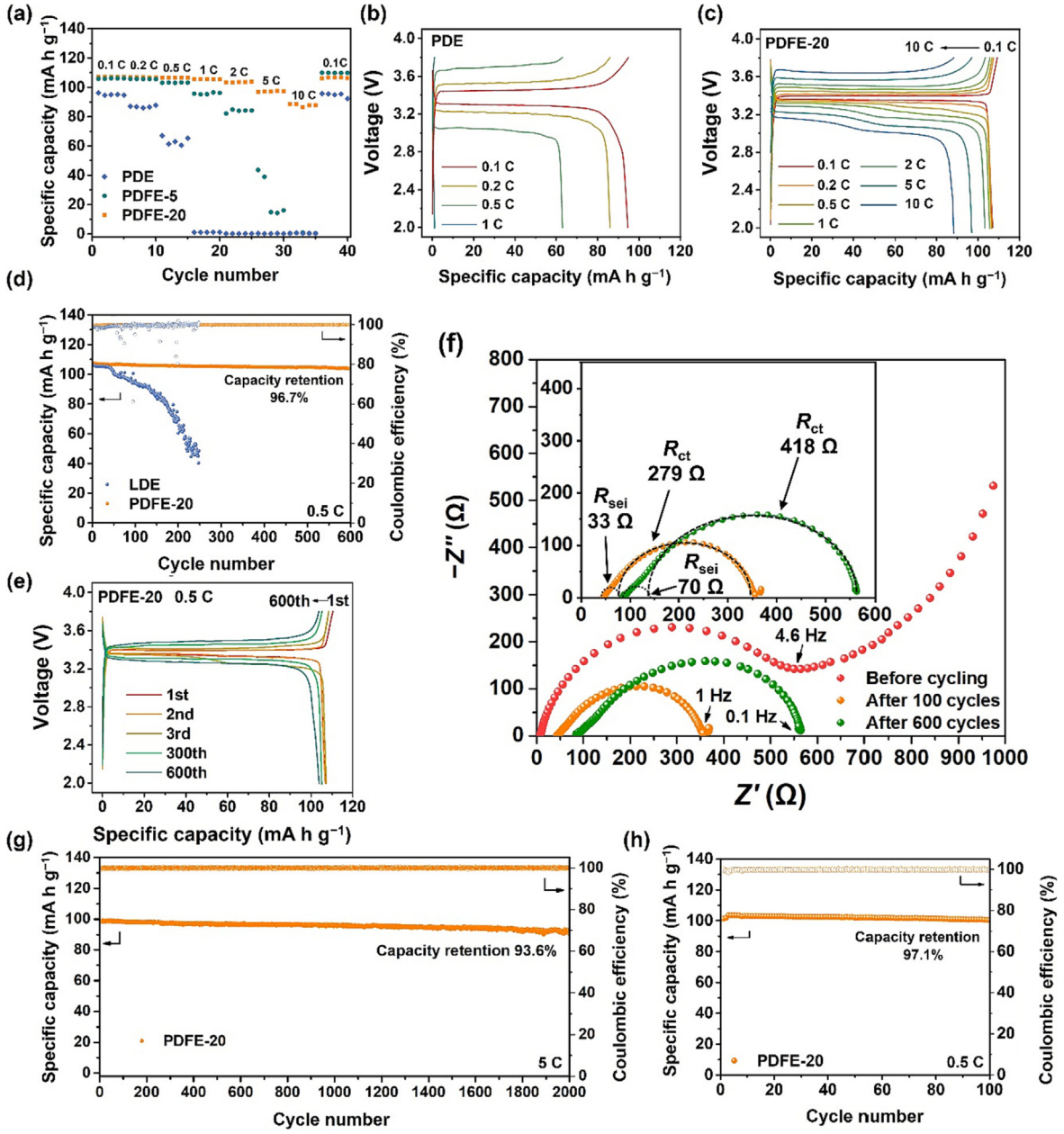

Fig. 6. Electrochemical performance of cells employing Na metal anode and an NVP cathode. (a) Comparison of rate performance of cells using PDE, PDFE-5 and PDFE-20. (b) Corresponding charge/discharge curves at different rates with PDE. (c) Corresponding charge/discharge curves at different rates with PDFE-20. (d) Comparison of long-term cycling performance of Na|PDFE-20|NVP and Na|LDE|NVP cells, cycled at 0.5 C. (e) Corresponding charge/discharge curves of the Na|PDFE-20|NVP cell. (f) Corresponding variation of Nyquist impedance spectra at different cycle numbers. (g) Long-term cycling performance of the Na|PDFE-20|NVP cell at a rate up to 5 C (585 mA g^{-1}). (h) Long-term cycling performance of the Na|PDFE-20|NVP cell at 0.5 C. The NVP mass loading in (a–g) is 1.12 mg cm^{-2}, and in (h) is 6.8 mg cm^{-2}.

facial resistance increases to 70 Ω and the charge transfer resistance increases to 418 Ω. These increases may be associated the gradual formation of additional NaF at the anode-electrolyte interface during cycling. There may also be slow ongoing reactions at the cathode-electrolyte interface.

Fig. 6(g) shows long-term cycling performance of the Na|PDFE-20|NVP cell, tested at current density up to 5 C (585 mA g^{-1}). The corresponding charge/discharge curves at different cycle numbers are presented in Fig. S14. It may be observed that the fast charge cycling behavior is stable, with a capacity retention of 93.6% after 2000 cycles, corresponding to a capacity loss of 0.0032% per cycle. To further evaluate this electrolyte, an NVP cathode with higher mass loading of active materials (6.8 mg cm^{-2}) was employed for the cycling test. Fig. 6(h) shows the cycling of a Na|PDFE-20|NVP coin-type cell at a rate of 0.5 C. Fig. S15 shows the corresponding charge/discharge curves at different cycle numbers. The cell can still stably cycle, with an initial discharge specific capacity of 104 mA h g^{-1} and a capacity retention of 97.1% after 100 cycles. Furthermore, based on the high mass-loading cathode, a Na|PDFE-20|NVP pouch-type cell is assembled for electrochemical evaluation. As shown in Fig. S16, the pouch cell possesses an initial discharge capacity of 105 mA h g^{-1} and will sustain 50 cycles at a charge/discharge rate of 0.5 C. To test the mechanical integrity of the electrolyte, the cell was bend 90° during the cycling. It was observed that the charge and discharge profiles remained unchanged, indicating good elastic flexibility of the cell. Table S3 provides a broad comparison of the electrochemical performance of full batteries with PDFE-20 and the leading published studies

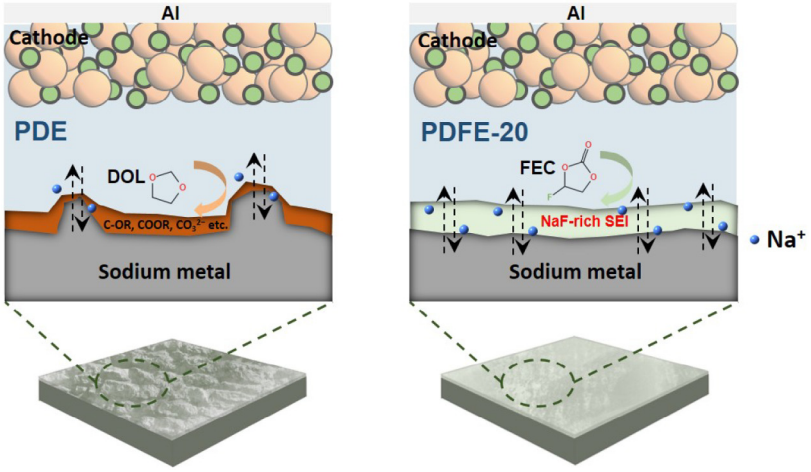

Scheme 1. Illustration of the key aspects of the plating/stripping processes with PDE-20 and baseline PDE.

on solid/quasi-solid electrolytes for SMBs employing NVP as the cathode. It may be observed that in terms of electrolyte's ionic conductivity as well as the battery's rate capability and cycling performance, the current results are among the most favorable.

In Scheme 1, the function of FEC in the poly(DOL)-FEC quasi-solid electrolyte is summarized. Poly(DOL)-based electrolytes have been widely employed in lithium metal/sulfur batteries. However, due to the higher reactivity of sodium over lithium, the continuous reactions between remnant unpolymerized DOL and Na metal result in an electrochemically unstable interface. The reaction products are mainly various organics with C—O, C═O and COOR bonds, that do not self-passivate the electrode. The FEC functions as an effective plasticizer so the bulk ionic conductivity is increased and the crystallinity of poly(DOL) is reduced. In parallel, a robust NaF-rich SEI layer is formed, which is known to stabilize the Na metal anode. The NaF-rich layer contributes to improved interfacial reaction kinetics that helps to homogenize sodium deposition and stripping, resulting in a flat rather than a roughened post-cycled interface. Significantly improved electrochemical performances are therefore obtained.

3. Conclusions

A novel high-performance quasi-solid polymer electrolyte for SMBs is created, being based on poly(DOL)–FEC–NaTFSI. The DOL polymerizes in-situ to form the polymer skeleton. The FEC functions as film-forming additive that improves ionic transport and stabilizes electrode–electrolyte interfaces. The electrolyte possesses an ionic conductivity as high as 3.31×10^{-3} S cm^{-1} at room temperature and an oxidation potential up to 4.4 V. A NaF-rich SEI layer forms on the surface of Na metal, which protects DOL from side reaction with Na metal, homogenizes the plating/stripping processes and inhibits the growth of dendrites. The Na||NVP cell (active material loading of 1.12 mg cm^{-2}) employing the poly (DOL)–FEC quasi-solid electrolyte displays an initial discharge capacity of 98.5 mA h g^{-1} and a capacity retention of 93.6% after 2000 cycles at a high rate of 5 C. When the active material loading is increased to 6.8 mg cm^{-2}, the cell still stably runs with an initial discharge capacity of 104 mA h g^{-1} and a capacity retention of 97.1% after 100 cycles at 0.5 C.

Experimental section

Experimental details can be found in the Supporting Information.

Declaration of competing interest

The authors declare that they have no known competing financial interests or personal relationships that could have appeared to influence the work reported in this paper.

Acknowledgments

All authors except P.L. and D.M. were financially supported by the National Natural Science Foundation of China (Grant Nos. 52072105 and 21676067), the Key R&D Program of Anhui Province (202104a05020044), the Anhui Provincial Natural Science Foundation (2108085J23), the Major Science and Technology Projects in Anhui Province (202003a05020014, 2021e03020001) and the Fundamental Research Funds for the Central Universities (PA2021KCPY0028, JZ2022HGTB0251). P.L. and D.M. (co-conception, research guidance, manuscript preparation) was supported by the National Science Foundation, Division of Materials Research, Award Number 1938833.

Appendix A. Supplementary data

Supplementary data to this article can be found online at https://doi.org/10.1016/j.jechem.2022.09.040.

References

[1] H.J. Liang, Z.Y. Gu, X.X. Zhao, J.Z. Guo, J.L. Yang, W.H. Li, B. Li, Z.M. Liu, W.L. Li, X. L. Wu, Angew. Chem. Int. Ed. 60 (2021) 26837–26846.
[2] Y. Huang, Z. Wang, M. Guan, F. Wu, R. Chen, Adv. Mater. 32 (2020) 2003534.
[3] C. Hakim, N. Sabi, I. Saadoune, J. Energy Chem. 61 (2021) 47–60.
[4] C. Zhao, L. Liu, X. Qi, Y. Lu, F. Wu, J. Zhao, Y. Yu, Y. Hu, L. Chen, Adv. Energy Mater. 8 (2018) 1703012.
[5] X. Yang, A.L. Rogach, Adv. Energy Mater. 10 (2020) 2000288.
[6] K. Pfeifer, S. Arnold, J. Becherer, C. Das, J. Maibach, H. Ehrenberg, S. Dsoke, ChemSusChem 12 (2019) 3312–3319.
[7] S. Wei, S. Choudhury, Z. Tu, K. Zhang, L.A. Archer, Acc. Chem. Res. 51 (2018) 80–88.
[8] Q. Zhang, Z. Wang, X. Li, H. Guo, J. Wang, G. Yan, Ionics 27 (2020) 683–691.
[9] J.F. Ding, R. Xu, X.X. Ma, Y. Xiao, Y.X. Yao, C. Yan, J.Q. Huang, Angew. Chem. Int. Ed. 61 (2022) e202115602.
[10] P.M.L. Le, T.D. Vo, H. Pan, Y. Jin, Y. He, X. Cao, H.V. Nguyen, M.H. Engelhard, C. Wang, J. Xiao, J.G. Zhang, Adv. Funct. Mater. 30 (2020) 2001151.
[11] W. Xia, Y. Zhao, F. Zhao, K. Adair, R. Zhao, S. Li, R. Zou, Y. Zhao, X. Sun, Chem. Rev. 122 (2022) 3763–3819.
[12] D. Wang, C. Zhu, Y. Fu, X. Sun, Y. Yang, Adv. Energy Mater. 10 (2020) 2001318.
[13] J. Ma, H. Jiang, L. Chen, Y. Wu, Y. Liu, W. Ping, X. Song, H. Xiang, J. Power Sources 537 (2022).

[14] S. Zhang, F. Zhao, S. Wang, J. Liang, J. Wang, C. Wang, H. Zhang, K. Adair, W. Li, M. Li, H. Duan, Y. Zhao, R. Yu, R. Li, H. Huang, L. Zhang, S. Zhao, S. Lu, T.K. Sham, Y. Mo, X. Sun, Adv. Energy Mater. 11 (2021) 2100836.
[15] L. Xu, Y. Lu, C.Z. Zhao, H. Yuan, G.L. Zhu, L.P. Hou, Q. Zhang, J.Q. Huang, Adv. Energy Mater. 11 (2021) 2002360.
[16] S. Lou, F. Zhang, C. Fu, M. Chen, Y. Ma, G. Yin, J. Wang, Adv. Mater. 33 (2021) 2000721.
[17] Y. Lu, C.Z. Zhao, H. Yuan, X.B. Cheng, J.Q. Huang, Q. Zhang, Adv. Funct. Mater. 31 (2021) 2009925.
[18] J.A. Lewis, F.J.Q. Cortes, Y. Liu, J.C. Miers, A. Verma, B.S. Vishnugopi, J. Tippens, D. Prakash, T.S. Marchese, S.Y. Han, C. Lee, P.P. Shetty, H. Lee, P. Shevchenko, F. De Carlo, C. Saldana, P.P. Mukherjee, M.T. McDowell, Nat. Mater. 20 (2021) 503–510.
[19] J. Liu, H. Yuan, H. Liu, C.Z. Zhao, Y. Lu, X.B. Cheng, J.Q. Huang, Q. Zhang, Adv. Energy Mater. 12 (2022) 2100748.
[20] Q. Ma, X.X. Zeng, J. Yue, Y.X. Yin, T.T. Zuo, J.Y. Liang, Q. Deng, X.W. Wu, Y.G. Guo, Adv. Energy Mater. 9 (2019) 1803854.
[21] J. Sun, X. Yao, Y. Li, Q. Zhang, C. Hou, Q. Shi, H. Wang, Adv. Energy Mater. 10 (2020) 2000709.
[22] J. Yi, D. Zhou, Y. Liang, H. Liu, H. Ni, L. Fan, J. Energy Chem. 58 (2021) 17–24.
[23] Z. Tong, S. Wang, A. Jena, C. Liu, S. Liao, J. Chen, H. Chang, S. Hu, X. Guo, R. Liu, ACS Appl. Mater. Interface 12 (2020) 44754–44761.
[24] X. Miao, H. Di, X. Ge, D. Zhao, P. Wang, R. Wang, C. Wang, L. Yin, Energy Storage Mater. 30 (2020) 170–178.
[25] H. Jiang, Y. Wu, J. Ma, Y. Liu, L. Wang, X. Yao, H. Xiang, J. Membr. Sci. 640 (2021).
[26] T. Ando, S. Yubuchi, A. Sakuda, A. Hayashi, M. Tatsumisago, Electrochemistry 87 (2019) 289–293.
[27] C. Wang, H. Xie, L. Zhang, Y. Gong, G. Pastel, J. Dai, B. Liu, E.D. Wachsman, L. Hu, Adv. Energy Mater. 8 (2018) 1701963.
[28] X. Cheng, C. Zhao, Y. Yao, H. Liu, Q. Zhang, Chem 5 (2019) 74–96.
[29] A. Banerjee, K.H. Park, J.W. Heo, Y.J. Nam, C.K. Moon, S.M. Oh, S. Hong, Y.S. Jung, Angew. Chem. Int. Ed. 128 (2016) 9786–9790.
[30] Y. Li, D. Zhang, X. Xu, Z. Wang, Z. Liu, J. Shen, J. Liu, M. Zhu, J. Energy Chem. 60 (2021) 32–60.
[31] Z. Li, H. Xie, X. Zhang, X. Guo, J. Mater. Chem. A 8 (2020) 3892–3900.
[32] Y. Wang, J. Ju, S. Dong, Y. Yan, F. Jiang, L. Cui, Q. Wang, X. Han, G. Cui, Adv. Funct. Mater. 31 (2021) 2101523.
[33] V. Vijayakumar, B. Anothumakkool, S. Kurungot, M. Winter, J.R. Nair, Energy Environ. Sci. 14 (2021) 2708–2788.
[34] J. Zhang, H. Wen, L. Yue, J. Chai, J. Ma, P. Hu, G. Ding, Q. Wang, Z. Liu, G. Cui, L. Chen, Small 13 (2017) 1601530.
[35] G. Chen, K. Zhang, Y. Liu, L. Ye, Y. Gao, W. Lin, H. Xu, X. Wang, Y. Bai, C. Wu, Chem. Eng. J. 401 (2020).
[36] S. Murugan, S.V. Klostermann, P. Schützendübe, G. Richter, J. Kästner, M.R. Buchmeiser, Adv. Funct. Mater. 32 (2022) 2201191.
[37] S. Chen, H. Che, F. Feng, J. Liao, H. Wang, Y. Yin, Z. Ma, ACS Appl. Mater. Interfaces 11 (2019) 43056–43065.
[38] T. Liu, J. Zhang, W. Han, J. Zhang, G. Ding, S. Dong, G. Cui, J. Electrochem. Soc. 167 (2020) 070527.
[39] F.Q. Liu, W.P. Wang, Y.X. Yin, S.F. Zhang, J.L. Shi, L. Wang, X.D. Zhang, Y. Zheng, J.J. Zhou, L. Li, Y.G. Guo, Sci. Adv. 4 (2018) eaat5383.
[40] W.P. Wang, J. Zhang, Y.X. Yin, H. Duan, J. Chou, S.Y. Li, M. Yan, S. Xin, Y.G. Guo, Adv. Mater. 32 (2020) 2000302.
[41] Q. Liu, B. Cai, S. Li, Q. Yu, F. Lv, F. Kang, Q. Wang, B. Li, J. Mater. Chem. A 8 (2020) 7197–7204.
[42] S. Wang, L. Zhou, M.K. Tufail, L. Yang, P. Zhai, R. Chen, W. Yang, Chem. Eng. J. 415 (2021) 128846.
[43] J. Wei, H. Yue, Z. Shi, Z. Li, X. Li, Y. Yin, S. Yang, ACS Appl. Mater. Interfaces 13 (2021) 32486–32494.
[44] Z. Geng, Y. Huang, G. Sun, R. Chen, W. Cao, J. Zheng, H. Li, Nano Energy 91 (2022) 106679.
[45] Q. Zhao, X. Liu, S. Stalin, K. Khan, L.A. Archer, Nat. Energy 4 (2019) 365–373.
[46] J. Xiang, Y. Zhang, B. Zhang, L. Yuan, X. Liu, Z. Cheng, Y. Yang, X. Zhang, Z. Li, Y. Shen, J. Jiang, Y. Huang, Energy Environ. Sci. 14 (2021) 3510–3521.
[47] G. Yang, Y. Zhai, J. Yao, S. Song, L. Lin, W. Tang, Z. Wen, N. Hu, L. Lu, Chem. Commun. 57 (2021) 7934–7937.
[48] W. Li, J. Gao, H. Tian, X. Li, S. He, J. Li, W. Wang, L. Li, H. Li, J. Qiu, W. Zhou, Angew. Chem. Int. Ed. 61 (2022) e202114805.
[49] P. Ding, Z. Lin, X. Guo, L. Wu, Y. Wang, H. Guo, L. Li, H. Yu, Mater. Today 51 (2021) 449–474.
[50] M. Li, Y. Liu, B. Qin, C. Lu, H.A. Butt, T. Zheng, D. Zhang, J. Alloys Compd. 861 (2021) 158647.
[51] H. Wu, G. Yu, L. Pan, N. Liu, M.T. McDowell, Z. Bao, Y. Cui, Nat. Commun. 4 (2013) 1943.
[52] M. Wu, D. Liu, D. Qu, J. Lei, X. Zhang, H. Chen, H. Tang, J. Colloid Interface Sci. 615 (2022) 627–635.
[53] C. Wang, H. Zhang, S. Dong, Z. Hu, R. Hu, Z. Guo, T. Wang, G. Cui, L. Chen, Chem. Mater. 32 (2020) 9167–9175.
[54] Z. Li, X. Zhou, X. Guo, Energy Storage Mater. 29 (2020) 149–155.
[55] A. Hosseinioun, E. Paillard, J. Membr. Sci. 594 (2020) 117456.
[56] S. Huang, Z. Cui, L. Qiao, G. Xu, J. Zhang, K. Tang, X. Liu, Q. Wang, X. Zhou, B. Zhang, G. Cui, Electrochim. Acta 299 (2019) 820–827.
[57] Z. Bi, W. Huang, S. Mu, W. Sun, N. Zhao, X. Guo, Nano Energy 90 (2021) 106498.
[58] C. Shu, J. Long, S.X. Dou, J. Wang, Small 15 (2019) 1804701.
[59] X. Chen, X. Shen, T. Hou, R. Zhang, H. Peng, Q. Zhang, Chem 6 (2020) 2242–2256.
[60] M. Zhu, S. Li, B. Li, Y. Gong, Z. Du, S. Yang, Sci. Adv. 5 (2019) eaau6264.
[61] J.A.S. Oh, J. Sun, M. Goh, B. Chua, K. Zeng, L. Lu, Adv. Energy Mater. 11 (2021) 2101228.
[62] X. Hu, E. Matios, Y. Zhang, C. Wang, J. Luo, W. Li, J. Energy Chem. 63 (2021) 305–311.
[63] X. Yu, A. Manthiram, Energy Storage Mater. 34 (2021) 282–300.
[64] J. Ma, Y. Wu, H. Jiang, X. Yao, F. Zhang, X. Hou, X. Feng, H. Xiang, Energy Environ. Mater. (2022), https://doi.org/10.1002/eem2.12370.
[65] C. Xu, G. Hernández, S. Abbrent, L. Kobera, R. Konefal, J. Brus, K. Edström, D. Brandell, J. Mindemark, ACS Appl. Energy Mater. 2 (2019) 4925–4935.
[66] D. Aurbach, E. Zinigrad, H. Teller, Y. Cohen, G. Salitra, H. Yamin, P. Dan, E. Elster, J. Electrochem. Soc. 149 (2002) A1267–A1277.
[67] G. Zhang, Z.W. Zhang, H.J. Peng, J.Q. Huang, Q. Zhang, Small Methods 1 (2017) 1700134.
[68] Y. Liu, R. Hu, D. Zhang, J. Liu, F. Liu, J. Cui, Z. Lin, J. Wu, M. Zhu, Adv. Mater. 33 (2021) 2004711.
[69] A. La Monaca, F. De Giorgio, F. Soavi, G. Tarquini, M. Di Carli, P. Paolo Prosini, C. Arbizzani, ChemElectroChem 5 (2018) 1272–1278.
[70] L. Kong, H. Zhan, Y. Li, Y. Zhou, Electrochem. Commun. 9 (2007) 2557–2563.
[71] X. Chen, X. Shen, B. Li, H.J. Peng, X.B. Cheng, B.Q. Li, X.Q. Zhang, J.Q. Huang, Q. Zhang, Angew. Chem. Int. Ed. 57 (2018) 734–737.
[72] X. Chen, H.R. Li, X. Shen, Q. Zhang, Angew. Chem. Int. Ed. 57 (2018) 16643–16647.
[73] X. Liu, X. Zheng, Y. Dai, W. Wu, Y. Huang, H. Fu, Y. Huang, W. Luo, Adv. Funct. Mater. 31 (2021) 2103522.
[74] J. Wu, J. Liu, Z. Lu, K. Lin, Y. Lyu, B. Li, F. Ciucci, J. Kim, Energy Storage Mater. 23 (2019) 8–16.
[75] Q. Yi, Y. Lu, X. Sun, H. Zhang, H. Yu, C. Sun, ACS Appl. Mater. Interfaces 11 (2019) 46965–46972.
[76] Y. Lee, J. Lee, J. Lee, K. Kim, A. Cha, S. Kang, T. Wi, S.J. Kang, H. Lee, N. Choi, ACS Appl. Mater. Interfaces 10 (2018) 15270–15280.
[77] B. Han, Y. Zou, Z. Zhang, X. Yang, X. Shi, H. Meng, H. Wang, K. Xu, Y. Deng, M. Gu, Nat. Commun. 12 (2021) 3066.
[78] D. Aurbach, E. Pollak, R. Elazari, G. Salitra, C.S. Kelley, J. Affinito, J. Electrochem. Soc. 156 (2009) A694–A702.
[79] J. Ma, F. Meng, Y. Yu, D. Liu, J. Yan, Y. Zhang, X. Zhang, Q. Jiang, Nat. Chem. 11 (2019) 64–70.
[80] Z. Xu, J. Yang, T. Zhang, L. Sun, Y. Nuli, J. Wang, S.I. Hirano, Adv. Funct. Mater. (2019) 1901924.
[81] E. Markevich, G. Salitra, D. Aurbach, ACS Energy Lett. 2 (2017) 1337–1345.
[82] R. Rodriguez, K.E. Loeffler, S.S. Nathan, J.K. Sheavly, A. Dolocan, A. Heller, C.B. Mullins, ACS Energy Lett. 2 (2017) 2051–2057.